Ti^{3+} Self-Doped Dark Rutile TiO_2 Ultrafine Nanorods with Durable High-Rate Capability for Lithium-Ion Batteries

*Jun Chen, Weixin Song, Hongshuai Hou, Yan Zhang, Mingjun Jing, Xinnan Jia, and Xiaobo Ji**

Dark-colored rutile TiO_2 nanorods doped by electroconducting Ti^{3+} have been obtained uniformly with an average diameter of ≈7 nm, and have been first utilized as anodes in lithium-ion batteries. They deliver a high reversible specific capacity of 185.7 mAh g^{-1} at 0.2 C (33.6 mA g^{-1}) and maintain 92.1 mAh g^{-1} after 1000 cycles at an extremely high rate 50 C with an outstanding retention of 98.4%. Notably, the coulombic efficiency of Ti^{3+}–TiO_2 has been improved by approximately 10% compared with that of pristine rutile TiO_2, which can be mainly attributed to its prompt electron transfer because of the introduction of Ti^{3+}. Again the synergetic merits are noticed when the promoted electronic conductivity is combined with a shortened Li^+ diffusion length resulting from the ultrafine nanorod structure, giving rise to the remarkable rate capabilities and extraordinary cycling stabilities for applications in fast and durable charge/discharge batteries. It is of great significance to incorporate Ti^{3+} into rutile TiO_2 to exhibit particular electrochemical characteristics triggering an effective way to improve the energy storage properties.

1. Introduction

Due to the increasing demand for electronic electric vehicles and hybrid electric vehicles, lithium-ion batteries (LIBs) are continuously attracting substantial research in designing satisfactory electrodes to meet the requirements of high energy/power densities and long lifespan.[1–3] Among various anode candidates, TiO_2 of different polymorphs has been studied intensively in recent years for its superior properties like low cost, abundance in nature, nonpollution, and most importantly, the cycling stability, which is derived from its neglectable volume expansion during Li-ion insertion–extraction processes.[4–6] Nevertheless, the practical application of TiO_2 as anodes in LIBs is severely hindered by its inferior rate capabilities resulting from both extremely poor electronic conductivity (10^{-13} S cm^{-1}) from the huge band gap (3.0 eV for anatase and 3.2 eV for rutile)[7] and sluggish lithium-ion diffusion (10^{-10}–10^{-17} cm^2 s^{-1}).[8–10] In terms of the enhancement of the rate capability, enormous research endeavor has been devoted to overcome these intrinsic drawbacks. One typical approach is focused on altering the morphologies like diminishing the particle to nanosize or designing novel micronanostructures such as nanotubes,[11] nanocubes,[12] and nanorods[13] to shorten the Li^+ diffusion length and enable faster Li^+ transport. Another effective strategy is aimed at improving electronic conductivity through cooperating with high conductive agents such as carbon materials[14–16] or doping alien atoms including N,[17–19] B,[20] Zn,[21] and Sn,[22] in which the doping method is greatly attractive on account that it not only benefits electron transfer but offers more open channels in a specific direction for Li^+ diffusion owing to the slight modification in the TiO_2 lattice.[21] However, note that the impurities' doping causes heterogeneous impurity defect, mostly followed by the decrease of thermal stability.[23]

In recent years, it has been reported that introducing Ti^{3+} or oxygen vacancies into TiO_2, usually displaying a black or dark color, can dramatically narrow the band gap to ≈1.54 eV and thus enhance the inherent electronic conductivity significantly,[24–26] which has drawn much interest mostly in photocatalysis. Meanwhile, since Shin et al.[27] reported the high-rate capabilities of oxygen-deficient $TiO_{2-\delta}$ via hydrogen reduction, which revealed that well-balanced Li^+/e^- transport is the key factor for high-performance TiO_2 anodes, the application of Ti^{3+}-doped TiO_2 for lithium storage has also been exploited in a blooming trend very recently. Nonetheless, in most reports, in order to produce Ti^{3+} or oxygen deficient into bulk TiO_2, especially with novel nanostructure morphologies, the particular-structured TiO_2 is prepared first, and then annealed in reducing atmosphere like H_2[25,28–30] and CO[31] or under vacuum condition,[32] which is harsh, tedious, and unsafe, and consequently limits its practical utilization. Indeed, some comparably mild tactics like hydrothermal method were developed to prepare Ti^{3+}-doped TiO_2 powder for lithium storage,[33,34] yet the morphologies of TiO_2 particles were difficult to control. Considering that the electrochemical properties of TiO_2 were largely dependent on its size and shape, especially for rutile phase, which is the most common natural form while Li insertion is usually reported to be negligible in micrometer size unless in nanosize,[35] it is desirable and significant to design the Ti^{3+} self-doped TiO_2 with fine nanostructure for high-rate performances through an alternative mild route.

J. Chen, W. Song, H. Hou, Y. Zhang, M. Jing, X. Jia, Prof X. Ji
College of Chemistry and Chemical Engineering
Central South University
Changsha 410083, P. R. China
E-mail: xji@csu.edu.cn

DOI: 10.1002/adfm.201502978

Herein, Ti^{3+} self-doped rutile TiO_2 nanorods exhibiting a dark color are efficiently obtained through a one-step solvothermal method and utilized as anode in LIBs for the first time, which combines the merits of the excellent conductivity from Ti^{3+} doping and shorter Li-ion migration pathways in uniformly dispersed ultrafine nanorods. The formation of TiO_2 nanorods and the introduction of Ti^{3+} are merged through one solvothermal procedure utilizing Mg powder as the reducing agent. The as-result dark TiO_2 as anode material in LIBs presents remarkable rate capabilities and excellent cycling performances even at high rates. The detailed structural and electrochemical studies are carried out to be informative for a profound and concise insight into the improved LIB performances of Ti^{3+} self-doped TiO_2.

2. Results and Discussion

2.1. Material Characterization

The crystal structure of the as-prepared dark TiO_2 (D-TiO_2) and white TiO_2 (W-TiO_2) was analyzed through XRD as shown in **Figure 1**. D-TiO_2 and W-TiO_2 exhibited similar diffraction peaks. The peak centers at 27.49°, 36.15°, 41.32°, 54.43°, and 69.16° were clearly observed, corresponding to (1 1 0), (1 0 1), (1 1 1), (2 1 1), and (3 0 1) crystal faces of tetragonal rutile TiO_2 indexed to the JCPDS card 87-0710 with a space group of P42/mnm ($a = b = 4.584$ Å and $c = 2.953$ Å). It was found that after annealing in air for 20 min, the positions of W-TiO_2 diffraction peaks did not shift and the peak intensities of the two samples were nearly identical, indicating that crystalline statuses of D-TiO_2 and W-TiO_2 were almost the same. Moreover, no other peaks resulting from impurities like Mg were observed, manifesting the Mg powder was removed totally after acid-washing and the pure TiO_2 of rutile phase was obtained. The visual photographs of TiO_2 were displayed near the corresponding X-ray diffraction (XRD) pattern, where the D-TiO_2 showed a dark gray color, and after high-temperature oxidation in air, it turned fully white as W-TiO_2.

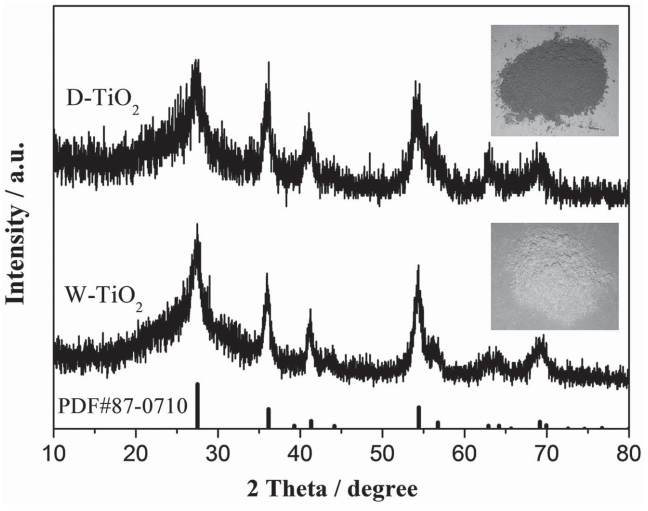

Figure 1. XRD patterns of D-TiO_2 and W-TiO_2 and their related visual photographs.

To clarify the chemical composition of the D-TiO_2 and W-TiO_2, X-ray photoelectron spectroscopy (XPS) was performed as exhibited in **Figure 2**. The survey scan of XPS (Figure 2a) showed a typical TiO_2 spectra and confirmed again the inexistence of impurities. The Ti 2p core-level XPS spectra were carried out in order to obtain detailed information on the chemical state of titanium ion in the two samples. As presented in Figure 2b, two major peaks at 458.1 and 463.9 eV were observed in the spectra of D-TiO_2, corresponding to the typical Ti^{4+} $2p_{3/2}$ and Ti^{4+} $2p_{1/2}$ peaks, respectively. Besides, the two shoulder peaks at 456.3 and 462.3 eV should be attributed to Ti^{3+} $2p_{3/2}$ and Ti^{3+} $2p_{1/2}$, revealing the existence of Ti^{3+} at TiO_2, which was in good accordance with the previous reports about Ti^{3+}-self doped TiO_2.[7,33,36] Since $TiCl_3$ solution was chosen as the starting agents to make the Ti^{3+} uniformly dispersed in the whole TiO_2 crystal, and Mg powder was employed as a strong reductant to avoid the oxidation of Ti^{3+}, while isopropanol was applied as the solvent where Ti^{3+} could survive well during solvothermal process, all of these successfully enable the presence of Ti^{3+} in the TiO_2 crystal as well as on the surface as depicted in Figure 2b. According to the Ti 2p XPS spectrum of D-TiO_2, a semiquantitative analysis of the sample was carried out and the Ti^{3+}/Ti^{4+} molar ratio of 0.141 was obtained. In contrast, as displayed in Figure 2c, there existed only two strong peaks at 458.5 and 464.3 eV of Ti^{4+} $2p_{3/2}$ and Ti^{4+} $2p_{1/2}$ in the Ti 2p XPS spectra of W-TiO_2, respectively. The two shoulder peaks disappeared and the Ti $2p_{3/2}$ and Ti $2p_{1/2}$ peaks shifted to higher binding energy, which were ascribed to the oxidation of Ti^{3+} to Ti^{4+} after annealing in air. As shown in Figure 2d, no peaks were found in the Mg 1s XPS spectrum of D-TiO_2, further confirming the absence of the Mg content in any form and definitely eliminating the possibility of Mg-doping in D-TiO_2.

Figure 3a displayed the representative low-resolution transmission electron microscopy (TEM) image of D-TiO_2, which exhibited that the well-defined nanorods were uniformly formed and finely dispersed. As shown in Figure 3b, after oxidation at 500 °C for 20 min, the morphology of TiO_2 nanorods was preserved mostly, while aggravation of a minor degree among the nanorods was observed as a result of the nanosized structures' fusion effects at high temperature.[37] It can be measured from Figure 3c that the lengths of D-TiO_2 nanorods for the most part were found to be ≈60 nm and the diameters were ≈7 nm, showing the ultrafine characteristic of the nanorods. For comparison, in the same resolution TEM of W-TiO_2 in Figure 3d, there were no obvious changes in the shape and size of nanorods between D-TiO_2 and W-TiO_2. Meanwhile, the smooth surface of D-TiO_2 was found to become comparably rough on W-TiO_2 after oxidation, which could be further verified by the high-resolution TEM (HRTEM) of a single nanorod in Figure 3e,f, where the structure boundary of W-TiO_2 was loose and irregular and there was a slight expansion in diameter after annealing, ascribed to the violent oxidation reaction between Ti^{3+} and oxygen and the fast escape of chemisorbed water and hydroxyl groups from TiO_2 crystal.[38] It was confirmed in Figure 3e,f that the diameter of the ultrafine nanorod was

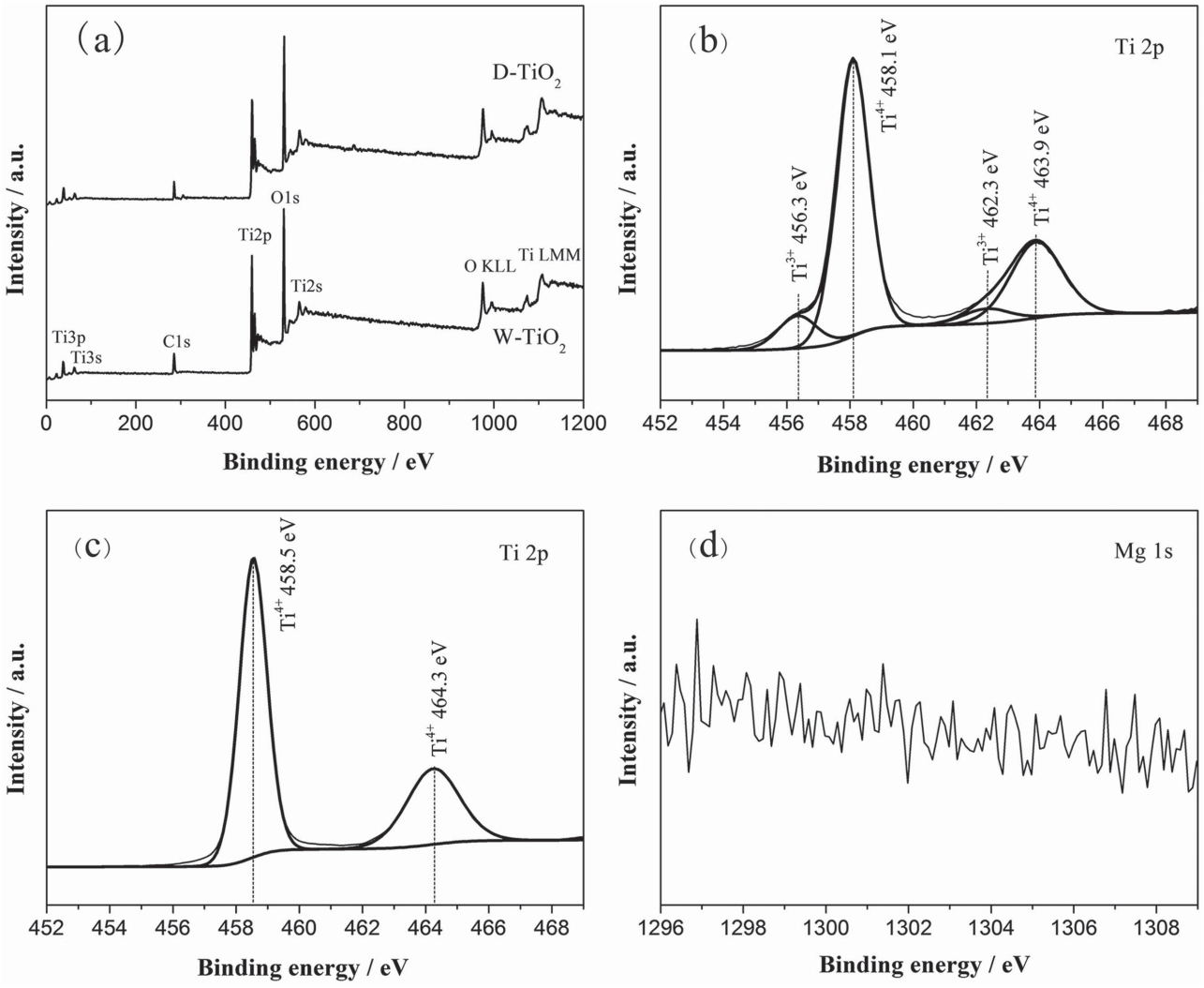

Figure 2. a) The survey scan of XPS of D-TiO_2 and W-TiO_2. b) Ti 2p XPS spectrum of D-TiO_2. c) Ti 2p XPS spectrum of W-TiO_2. d) Mg 1s XPS spectrum of D-TiO_2.

6–7 nm and the lattice fringes were approximately 0.32 nm, revealing the lattice plane of (1 1 0) of crystalline D-TiO_2 and W-TiO_2.

2.2. Electrochemical Properties

The electrochemical performances of the as-prepared samples as anode material for LIBs were investigated and the typical cyclic voltammograms (CVs) at a scan rate of 0.1 mV s^{-1} between 1 and 3 V (vs Li/Li^+) of the obtained D-TiO_2 and W-TiO_2 were shown in **Figure 4**a,b, respectively. The initial three cycles of the two samples both exhibited one couple of broad redox peaks at 1.45 V (peak A) for reductive peak and 1.95 V (peak B) for oxidative one, which were the typical feature of lithium intercalation/deintercalation into/from nanosized rutile TiO_2. On the first cathodic sweep, the very broad peak at around 2.0 V (peak C) was associated with the breakdown of the electrolyte impurities,[39] which was typically irreversible. Besides, the deviation of the curves was mainly due to the chemisorbed water and surface hydroxyl groups of the unannealed D-TiO_2. The current intensity of the initial peak at 1.45 V decreased rapidly compared with that of cathodic peaks in the following two cycles, as a result of the irreversible formation of the Li_xTiO_2 phase from the fresh rutile phase, which consumed some TiO_2 and passivated the interfaces.[40] Notably, the variation of the current density between the initial cathodic peak and the next two of D-TiO_2 electrodes was smaller than that of W-TiO_2, implying the better reversibility of D-TiO_2.

The galvanostatic charge–discharge potential curves were obtained at a current density of 0.2 C (equal to 33.6 mA g^{-1}) as shown in **Figure 5**a,b for D-TiO_2 and W-TiO_2, respectively. The original open-circuit voltage of the two batteries were both approximately 3.0 V versus Li/Li^+, while the voltage drop trend from 3.0 to 1.5 V in the initial discharge curve (marked as region A in Figure 5a,b) varied between D-TiO_2 and W-TiO_2 electrodes. For W-TiO_2 in Figure 5b, which was a typically

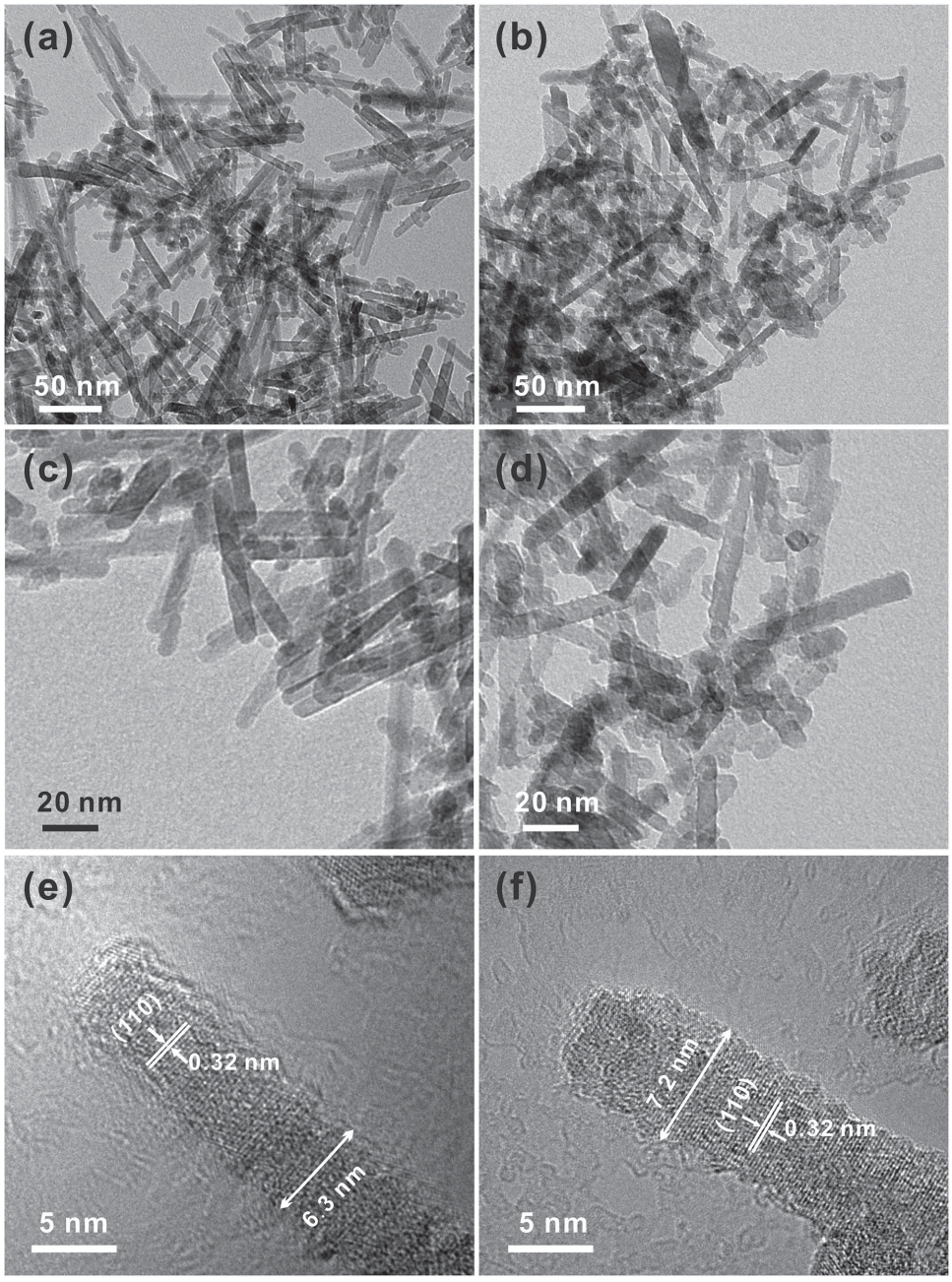

Figure 3. TEM images of a,c) D-TiO_2 and b,d) W-TiO_2. HRTEM images of e) D-TiO_2 and f) W-TiO_2.

featured discharge curve of rutile TiO_2, it could be observed that the voltage decreased from 3.0 to 2.4 V rapidly and then to 1.5 V monotonously, corresponding to the storage of 0.18 mol Li^+ per mole of W-TiO_2, which was a common phenomenon related to the decrease in particle and crystallite size for the nanomaterials.[41] In contrast, it was interesting that in region A of Figure 5a, the voltage dropped much more slowly than that of W-TiO_2 and as high as 0.36 mol Li^+ was able to be accommodated in D-TiO_2. It was known that the discharge process in region A was mainly due to the homogeneous insertion of Li^+ in the interface of rutile,[42] which was reported to be associated with the size effects that the potential profiles tended to become flatter initially when the grain size was smaller than the width of the space-charge zones linked to the electrical properties in the ionic charge carriers.[43,44] Since the grain size of D-TiO_2 and W-TiO_2 nanorods were similar as proved in TEM and HRTEM in Figure 3, the variation of electrochemical behavior in region A of Figure 5a,b could be probably attributed to the different electrical properties of D-TiO_2 and W-TiO_2 resulting from the dispersion of Ti^{3+} in the D-TiO_2 nanocrystal. It should also be noted that the short plateau appeared at approximately 1.45 V in the first discharge curve in Figure 5a,b as a result of Li ions occupying its octahedral position, which was in accordance with the initial cathodic peak in CV tests. That plateau

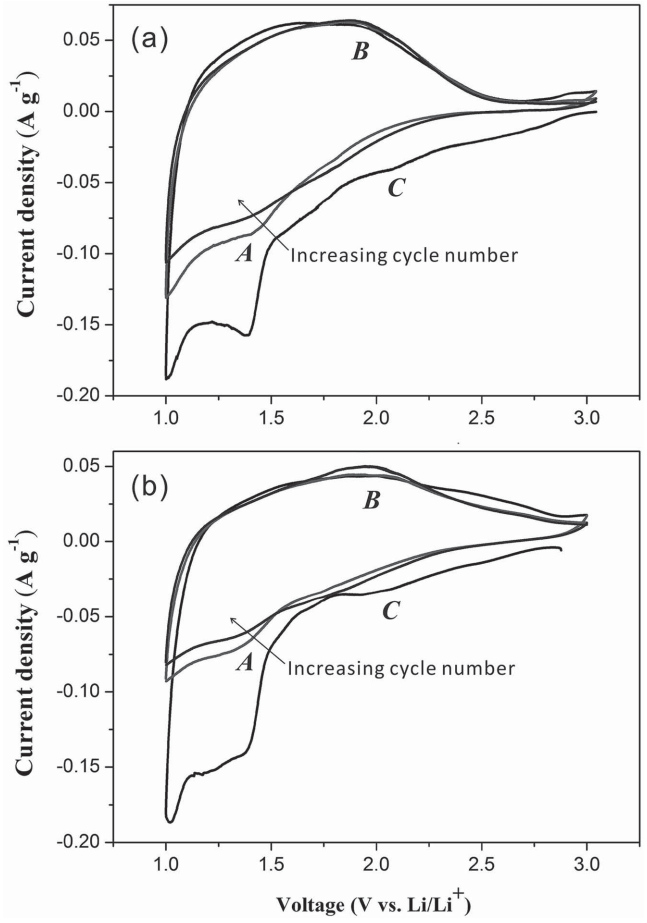

Figure 4. Cyclic voltammograms of a) D-TiO_2 and b) W-TiO_2 at the scan rate of 0.1 mV s^{-1} in a voltage range of 1–3 V versus Li/Li^+.

appeared to be a sloped region during the following discharge curves as a result of the irreversible formation of a "nanocomposite" of crystalline grains and amorphous regions[42,45] The large initial discharge-specific capacity of 282.4 mAh g^{-1} for D-TiO_2 and 315.5 mAh g^{-1} for W-TiO_2 were obtained, and the charge-specific capacity of 198.4 and 192.4 mAh g^{-1} could be delivered, respectively. Apparently, the initial coulombic efficiency of D-TiO_2 (70.3%) was higher than that of D-TiO_2 (60.8%), where the increase of nearly 10% suggested the better reversibility of D-TiO_2 electrode, which was in agreement with the CV outcome. The enhancement of coulombic efficiency might be derived from the distinctive chemical composition and promoted electron transportation of Ti^{3+} doped D-TiO_2. It has been proved that microsized rutile particles were able to host only negligible amount of Li^+ and the Li insertion capacity could be strongly increased by the nanosizing, especially for the ultrasmall nanosize under 12 nm.[39,42,46] During the following two cycles, it was found that nearly 0.57 mol Li^+ could be reversibly accommodated to form $Li_{0.57}TiO_2$ (189.5 mAh g^{-1}) in D-TiO_2 and 0.55 mol Li^+ (184.7 mAh g^{-1}) in W-TiO_2 during discharge process, of which the large storage capacity could be attributed to the downsize of rutile crystalline grains to ultrafine nanometers. The rate capabilities of the two samples were obtained from the reversible charge and discharge profiles at different rates as displayed in Figure 5c,d. For D-TiO_2, as the current density increased from 0.2 C to 80 C, the discharge–charge profile shapes were well preserved, and the charge-specific capacities of 185.7, 166.7, 154.6, 135.5, and 123.4 mAh g^{-1} were yielded at the rates of 0.2 C, 1 C, 2 C, 5 C, and 10 C, respectively. Moreover, even charged/discharged at high rates of 20 C, 50 C, and 80 C, D-TiO_2 was still able to deliver a charge-specific capacity of 111.7, 93.6, and 76.8 mAh g^{-1} with a retention of 60.1%, 50.4%, and 41.6%, separately, compared with that at 0.2 C, indicating the remarkable high-rate performance of D-TiO_2 in a LIB. For W-TiO_2, it could exhibit a charge-specific capacity of 180.8 mAh g^{-1} at 0.2 C, almost equal to that of D-TiO_2, whereas the capacities dropped quickly to 149.3, 128.7, 97.6, 71.5, and 50.4 mAh g^{-1} at 1 C, 2 C, 5 C, 10 C, and 20 C, respectively.

The excellent rate performances of D-TiO_2 nanorods could be ascribed to the combined impacts of the ultrafine nanorods structure and the introduction of Ti^{3+} species. First, it has reported that during the charge/discharge process, the effective diffusion length for Li^+ ion is 24–240 nm at the rate of 1 C, and 3.2–32 nm at 60 C.[47] Thereby, larger capacity could be obtained at high rates if the particle diameter of the electrode material can be reduced smaller than the lengths above, by which the great advantage of the ultrafine nanostructure could be fully expressed. Here, the average diameter of the well-dispersed D-TiO_2 nanorods was ≈7 nm, which could remarkably shorten the Li^+ diffusion length, especially in the high rate and benefit large Li^+ flux. On the other hand, the electronic conductivity of TiO_2 was enhanced significantly by the Ti^{3+}-doping, which could enable fast electron transfer even at high rates. Since the electrochemical reaction of TiO_2 with Li^+ could occur only when equivalent electrons and Li ions are available simultaneously,[27,48] the synergetic merits of the fast electron transport and shortened Li^+ diffusion distance of ultrafine D-TiO_2 nanorods could further facilitate the Li^+ storage and prompt the outstanding high-rate performances.

The cycling performances of D-TiO_2 and W-TiO_2 at the rate of 1 C (167.5 mA g^{-1}) were depicted in **Figure 6**a. The initial reversible charge-specific capacity of D-TiO_2 was 168.8 mAh g^{-1}, and after 300 discharge–charge cycles at 1 C, the specific capacity remained 162.5 mAh g^{-1} with the retention of 96.3%. Referring to W-TiO_2, a specific capacity of 152.9 mAh g^{-1} was obtained initially and retained 129.0 mAh g^{-1} after 300 cycles at 1 C, corresponding to the capacity retention of 84.4%. Comparatively speaking, D-TiO_2 could exhibit more excellent cycling stability. In addition, the initial coulombic efficiency of D-TiO_2 and W-TiO_2 were 72.6% and 65.4%, respectively, both of which climbed to 99.0% in the first three cycles and kept over 99.5% steadily during 300 cycles, revealing the favorable reversibility of the two rutile samples after the first cycle. The rate performances of the D-TiO_2 and W-TiO_2 were further compared clearly in Figure 6b. The cell was initially cycled at 0.2 C, and the charge capacity decreased in the original seven cycles. In the subsequent cycles, the capacities were stable at each rate for five cycles. It was evident that D-TiO_2 exhibited much more improved rate performances than the pure rutile W-TiO_2. To evaluate the cyclability at high rate, after the rate test, D-TiO_2 electrode was sequentially discharged–charged

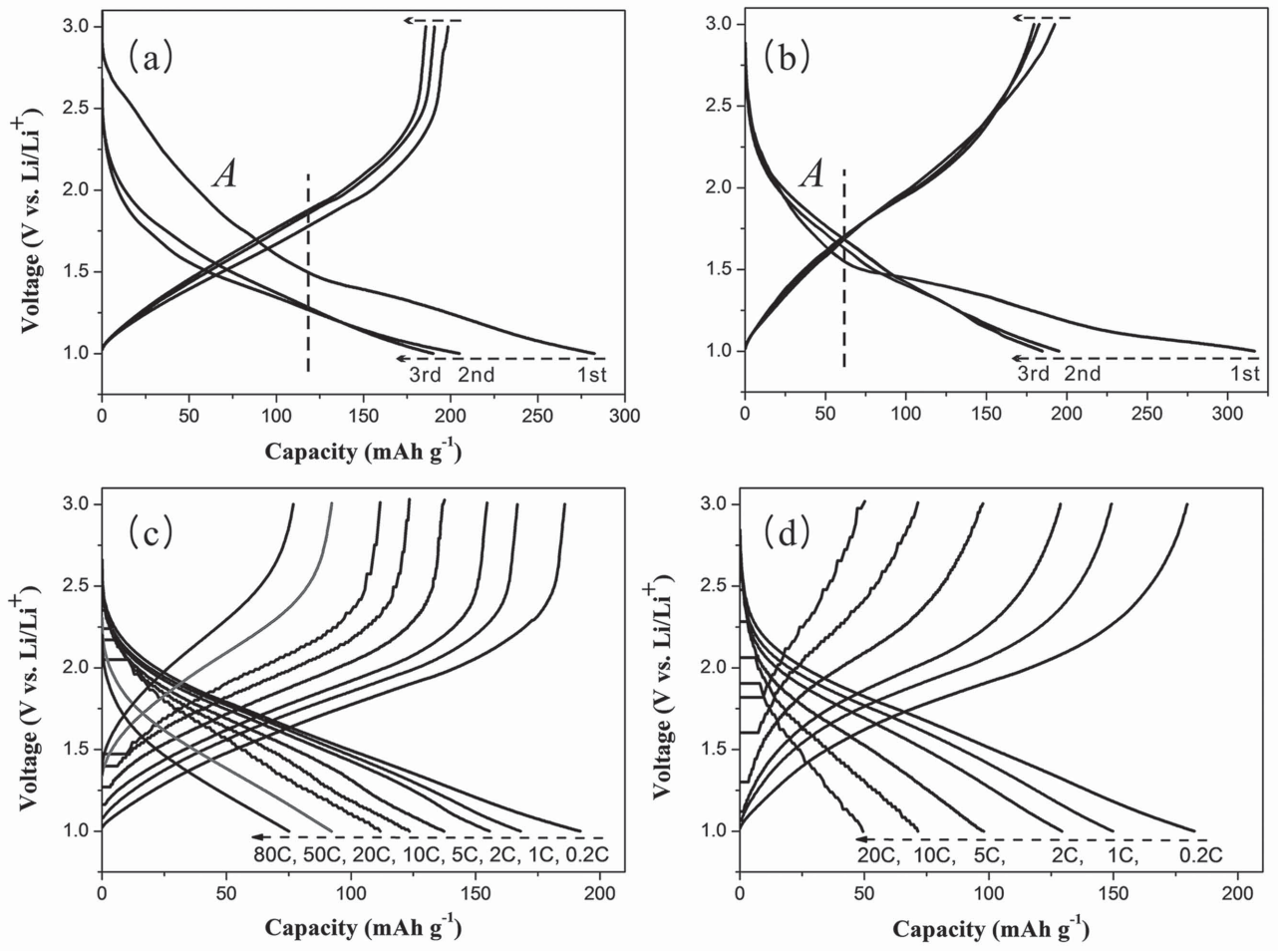

Figure 5. Charge and discharge profiles of a) D-TiO_2 and b) W-TiO_2 of different cycles at a rate of 0.2 C. Reversible charge and discharge profiles of c) D-TiO_2 at different rates from 0.2 C to 80 C and d) W-TiO_2 at different rates from 0.2 C to 20 C (1 C = 168 mA g^{-1})

at 50 C over 1000 cycles. It could be clearly seen in Figure 6c that D-TiO_2 retained a charge capacity of 92.1 mAh g^{-1} after 1000 cycles at 50 C, holding a capacity retention of as high as 98.4%. Moreover, the coulombic efficiency sustained almost 100% during the 1000 cycles, further confirming the excellent durability of the electrode. Compared with the rutile anode materials reported so far (**Table 1**), the as prepared D-TiO_2 here exhibited outstanding cycling stability and extraordinary rate capabilities.

In order to analyze and compare the electrochemical impedance in the D-TiO_2 and W-TiO_2 battery, electrochemical impedance spectroscopy (EIS) was further employed on the battery, which had been tested after 10 cycles at the rate of 0.2 C and charged to the same voltage of 2.0 V. The Nyquist plots were presented in **Figure 7** and the inset figure depicted its corresponding fitting equivalent circuit. The chi-squared function was less than 10^{-4} in this study, which certified that the credibility of the fitting equivalent since the value of chi-squared function between 10^{-5} and 10^{-4} was proved to provide a reasonably good indication of the quality of the fit.[49,50] All the fitting results and relative errors estimate (%) are listed in **Table 2**, where the small intercept at the Z' axis denoted as R_s showed the internal resistance of electrode and electrolyte in the battery while the semicircle in the intermediate frequency region corresponding to $R1$ represented charge-transfer impedance on the interface of the electrode–electrolyte.[51,52] The sloping line in the low-frequency region related to $W1$, namely Warburg impendence, signified the solid-state diffusion resistance. CPE1 was related to the surface property of the electrode and $C1$ manifested the capacitance caused by ion transfer in the electrode material. It could be seen from the table that the internal resistance of electrode and electrolyte (R_s) of D-TiO_2 was as small as that of W-TiO_2 after cycled at the same condition for 10 times, while the charge transfer impedance ($R1$) of D-TiO_2 electrode was 48.35 Ω cm^{-2}, which was much lower than that of W-TiO_2 (75.6 Ω cm^{-2}), indicating an enhanced charge transfer on the electrode–electrolyte, owing to the introduction of Ti^{3+} which has considerably improved the electrical conductivity of the TiO_2 nanorods.

3. Conclusion

The Ti^{3+} self-doped rutile TiO_2 nanorods presenting a dark color as anode material in LIBs were successfully prepared by a facile solvothermal method utilizing easily accessible Mg

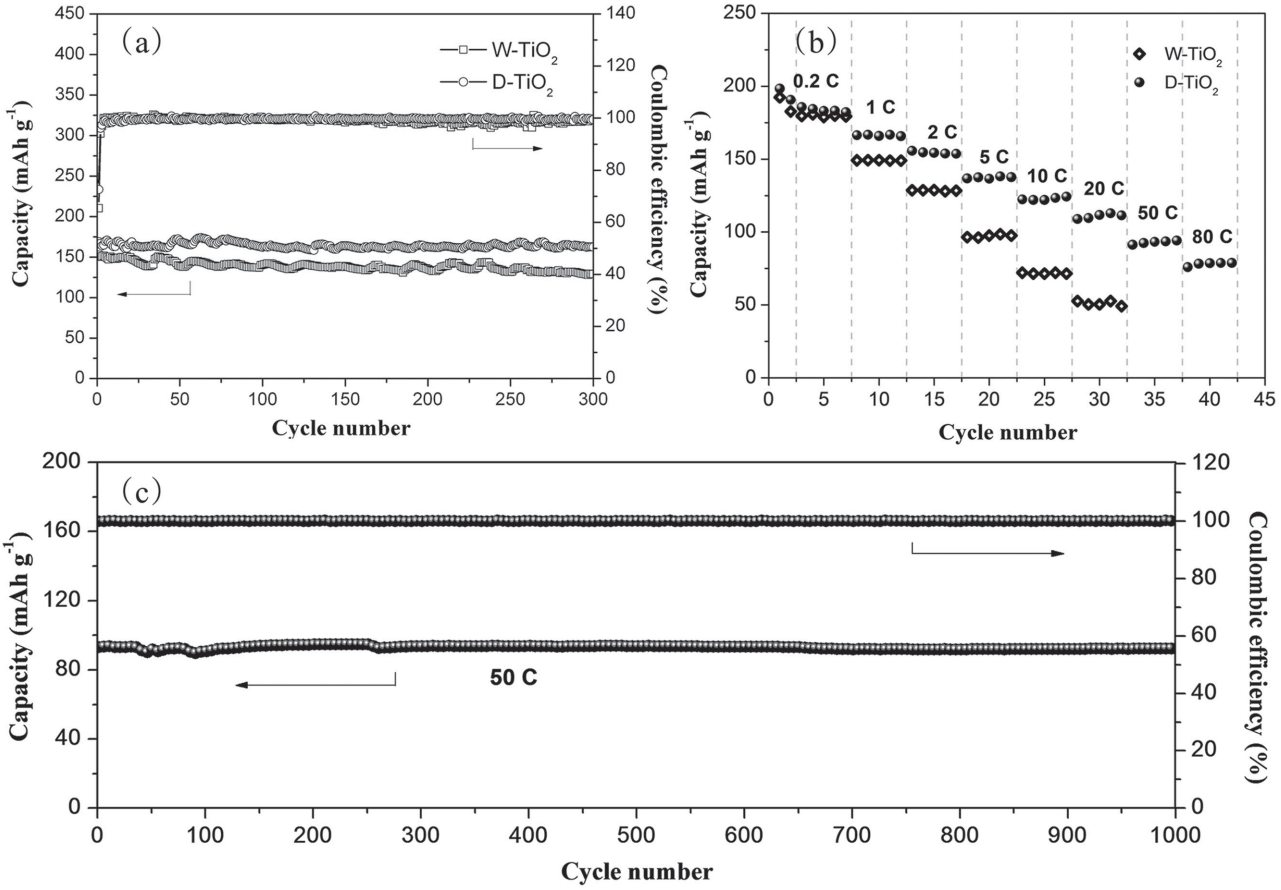

Figure 6. a) The cycling performances of D-TiO_2 and W-TiO_2 at the rate of 1 C. b) The rate capabilities of D-TiO_2 and W-TiO_2 at various rates. c) The cycling performance of D-TiO_2 at the rate of 50 C showed by Li^+ extraction capacity and coulombic efficiency versus cycle number.

powder as the reducing agent and $TiCl_3$ as the Ti^{3+} source. The as-obtained uniformly dispersed Ti^{3+}–TiO_2 nanorods with an average diameter of ≈7 nm demonstrated remarkable rate capabilities and excellent high-rate long-term cycling stability. They delivered a high reversible specific capacity of 185.7 mAh g^{-1} at the current density of 0.2 C (33.5 mA g^{-1}), and still exhibited 93.6 mAh g^{-1} at the high rate of 50 C (8.38 A g^{-1}), which is far superior to the oxidized white rutile TiO_2, and after 1000 cycles at 50 C, a capacity retention of as high as 98.4% was obtained. Their considerably enhanced durable high-rate performance was attributed to the improved electronic conductivity resulting from the introduction of Ti^{3+} and the shortened Li^+ diffusion length because of the ultrafine nanorod structure. It is anticipated that the dark Ti^{3+} self-doped rutile TiO_2 nanorods can be employed as a promising candidate for anode materials for fast and durable LIBs.

Table 1. Comparison of the electrochemical performances of the as-prepared rutile D-TiO_2 with previously reported rutile TiO_2 anode materials for LIBs.

Materials	10 C Capacity [mAh g^{-1}]	50 C Capacity [mAh g^{-1}]	Cycling capacity retention
TiO_2 submicroboxes[53]	115	68 (30 C)	89.5% over 200 cycles (1 C)
			96.6% over 500 cycles (5 C)
TiO_2 mesocrystals[13]	100 (5C)	–	82.6% over 100 cycles (1 C)
Nanosized TiO_2[42]	100	70 (30 C)	–
TiO_2 mesocrystals[54]	≈100	76.5 (20 C)	77% over 100 cycles (1 C)
TiO_2/graphene[55]	≈115	87 (30 C)	94% over 100 cycles (1 C)
B-doped TiO_2[20]	72	–	86% over 300 cycles (2 C)
TiO_2 microspheres[56]	106	–	95.8% over 100 cycles (1 C)
Dark TiO_2 nanorods (this work)	**123**	**93.6**	**96.3% over 300 cycles (1 C)**
			98.4% over 1000 cycles (50 C)

4. Experimental Section

Materials Preparation: Ti^{3+} doped dark rutile TiO_2 nanorods (D-TiO_2) were prepared through solvent-thermal method. Typically, 0.12 g Mg powder (Xilong Chemical Co., Ltd.) was dispersed into 30 mL isopropanol (Sinopharm Chemical Reagent Beijing Co., Ltd.) under magnetic stirring at room temperature (25 °C), followed by adding 1 mL $TiCl_3$ (15%–20%, Sinopharm Chemical Reagent Beijing Co., Ltd.). The resulting mixture was kept stirring for 20 min when the color turned from violet to dusty blue, and then transferred in a dried Teflon autoclave, maintaining at 180 °C for 6 h. After being cooled to room temperature, the precipitate was collected by centrifuge, washed with ethanol for

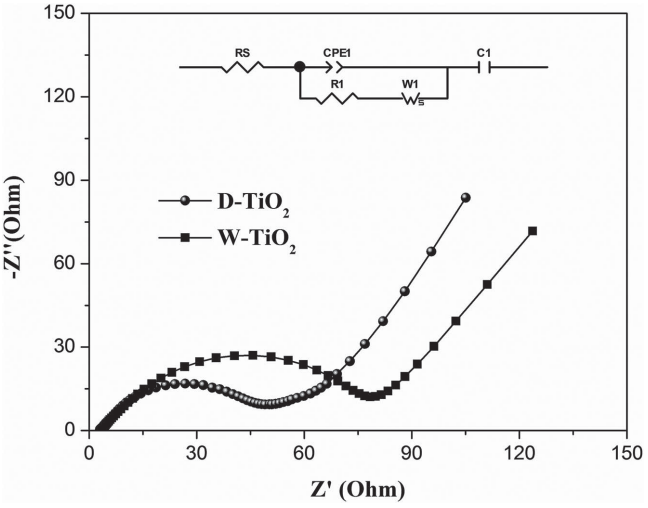

Figure 7. Electrochemical impedance spectroscopy of D-TiO_2 and W-TiO_2 after 10 cycles at the rate of 0.2 C and the inset figure presents the corresponding equivalent circuit.

several times, then dispersed in 100 mL of 2 M HCl aqueous solution (Sinopharm Chemical Reagent Beijing Co., Ltd.) under vigorous stirring for 10 h, and further washed with deionized water repeatedly. After dried at 60 °C in a vacuum oven, the dark-gray TiO_2 powder was obtained, named D-TiO_2. For comparison, the D-TiO_2 was calcined in air at 500 °C for 20 min to prepare the white TiO_2, named W-TiO_2.

Materials Characterization: Powder XRD was performed on powdered samples using a Bruker D8 diffractometer with monochromatic Cu Kα radiation (λ = 1.5406 Å), and the diffraction data was recorded in the 2θ range of 10°–60° with a scan rate of 8° min^{-1}. FEI Quanta 200 scanning electron microscopy, JEM-2100F TEM, and K-Alpha 1063 XPS were used to characterize the morphology and composition of the samples.

Electrochemical Tests: Electrochemical tests were operated using CR2016 coin-type cells, consisting of the cathode and a lithium metal anode, separated by a porous polyethylene film (Celgard 2500). The cathode contained 70% active material, 15% super P as conductive additive, and 15% carboxymethyl cellulose as binder. The slurry was coated onto copper foil and dried at 80 °C for 12 h in a vacuum oven. The coin cell was assembled in an Ar-filled MBraun glovebox. The electrolyte was 1 M $LiPF_6$ dissolved in a mixture of ethylene carbonate, dimethyl carbonate, and diethyl carbonate (1:1:1 by volume). For each coin cell, the mass loading of the active material is about 1.0–1.2 mg. Cyclic voltammetry and galvanostatic charge/discharge cycling tests were carried out in a setting voltage range by using Solartron Analytical and Arbin battery cycler (BT2000), respectively. EIS was studied using a Zahner IM6e. The impedance spectrum was recorded using an AC voltage of 5 mV in the frequency range from 1 to 10 mHz. All electrochemical tests were carried out at room temperature.

Table 2. Impedance parameters of the fitting equivalent circuit.

	R_s [Ω cm^{-2}]	CPE1 [S $s^{1/2}$ cm^{-2}]	$R1$ [Ω cm^{-2}]	$W1$ [S $s^{0.5}$ cm^{-2}]	$C1$ [F cm^{-2}]
$Results_D$	3.263	1.359×10^{-4}	48.35	0.01171	0.0534
$Error_D$ (%)	2.125	4.089	2.287	3.249	8.09
$Results_W$	3.561	8.019×10^{-5}	75.6	0.0198	0.996
$Error_W$ (%)	1.756	3.032	2.27	5.76	10.3

Acknowledgements

This work was financially supported by the National Natural Science Foundation of China (21473258), the Program for the New Century Excellent Talents in University (NCET-11-0513), the Distinguished Young Scientists of Hunan Province (13JJ1004), Natural Science Foundation of Hunan (2014GK2016), and Hunan Provincial Innovation Foundation for Postgraduate (CX2015B039).

Received: July 17, 2015
Revised: September 15, 2015
Published online: October 7, 2015

[1] B. Kang, G. Ceder, *Nature* **2009**, *458*, 190.
[2] M. Reddy, G. Subba Rao, B. Chowdari, *Chem. Rev.* **2013**, *113*, 5364.
[3] V. Etacheri, R. Marom, R. Elazari, G. Salitra, D. Aurbach, *Energy Environ. Sci.* **2011**, *4*, 3243.
[4] D. Deng, M. G. Kim, J. Y. Lee, J. Cho, *Energy Environ. Sci.* **2009**, *2*, 818.
[5] X. Chen, S. S. Mao, *Chem. Rev.* **2007**, *107*, 2891.
[6] T. Froschl, U. Hormann, P. Kubiak, G. Kucerova, M. Pfanzelt, C. K. Weiss, R. J. Behm, N. Husing, U. Kaiser, K. Landfester, M. Wohlfahrt-Mehrens, *Chem. Soc. Rev.* **2012**, *41*, 5313.
[7] G. Li, Z. Lian, X. Li, Y. Xu, W. Wang, D. Zhang, F. Tian, H. Li, *J. Mater. Chem. A* **2015**, *3*, 3748.
[8] I. Moriguchi, R. Hidaka, H. Yamada, T. Kudo, H. Murakami, N. Nakashima, *Adv. Mater.* **2006**, *18*, 69.
[9] I. Abayev, A. Zaban, F. Fabregat-Santiago, J. Bisquert, *Phys. Status Solidi A* **2003**, *196*, R4.
[10] S. Moitzheim, C. S. Nimisha, S. Deng, D. J. Cott, C. Detavernier, P. M. Vereecken, *Nanotechnology* **2014**, *25*, 504008.
[11] S. Brutti, V. Gentili, H. Menard, B. Scrosati, P. G. Bruce, *Adv. Energy Mater.* **2012**, *2*, 322.
[12] X. Yang, Y. Yang, H. Hou, Y. Zhang, L. Fang, J. Chen, X. Ji, *J. Phys. Chem. C* **2015**, *119*, 3923.
[13] Z. Hong, M. Wei, T. Lan, L. Jiang, G. Cao, *Energy Environ. Sci.* **2012**, *5*, 5408.
[14] J. Chen, H. Hou, Y. Yang, W. Song, Y. Zhang, X. Yang, Q. Lan, X. Ji, *Electrochim. Acta* **2015**, *164*, 330.
[15] D. Bresser, B. Oschmann, M. N. Tahir, F. Mueller, I. Lieberwirth, W. Tremel, R. Zentel, S. Passerini, *J. Electrochem. Soc.* **2015**, *162*, A3013.
[16] R. Mo, Z. Lei, K. Sun, D. Rooney, *Adv. Mater.* **2014**, *26*, 2084.
[17] Y. Zhang, F. Du, X. Yan, Y. Jin, K. Zhu, X. Wang, H. Li, G. Chen, C. Wang, Y. Wei, *ACS Appl. Mater. Interfaces* **2014**, *6*, 4458.
[18] Y. Yang, X. Ji, M. Jing, H. Hou, Y. Zhu, L. Fang, X. Yang, Q. Chen, C. E. Banks, *J. Mater. Chem. A* **2015**, *3*, 5648.
[19] L. Tan, L. Pan, C. Cao, B. Wang, L. Li, *J. Power Sources* **2014**, *253*, 193.
[20] H. Tian, F. Xin, X. Tan, W. Han, *J. Mater. Chem. A* **2014**, *2*, 10599.
[21] Z. Ali, S. N. Cha, J. I. Sohn, I. Shakir, C. Yan, J. M. Kim, D. J. Kang, *J. Mater. Chem.* **2012**, *22*, 17625.
[22] M. Lübke, I. Johnson, N. M. Makwana, D. Brett, P. Shearing, Z. Liu, J. A. Darr, *J. Power Sources* **2015**, *294*, 94.
[23] R. Asahi, T. Morikawa, T. Ohwaki, K. Aoki, Y. Taga, *Science* **2001**, *293*, 269.
[24] X. Chen, L. Liu, F. Huang, *Chem. Soc. Rev.* **2015**, *44*, 1861.
[25] X. Chen, L. Liu, Y. Y. Peter, S. S. Mao, *Science* **2011**, *331*, 746.
[26] A. Naldoni, M. Allieta, S. Santangelo, M. Marelli, F. Fabbri, S. Cappelli, C. L. Bianchi, R. Psaro, V. Dal Santo, *J. Am. Chem. Soc.* **2012**, *134*, 7600.
[27] J.-Y. Shin, J. H. Joo, D. Samuelis, J. Maier, *Chem. Mater.* **2012**, *24*, 543.

[28] Y. Yan, B. Hao, D. Wang, G. Chen, E. Markweg, A. Albrecht, P. Schaaf, *J. Mater. Chem. A* **2013**, *1*, 14507.
[29] J.-Y. Eom, S.-J. Lim, S.-M. Lee, W.-H. Ryu, H.-S. Kwon, *J. Mater. Chem. A* **2015**, *3*, 11183.
[30] F. Zuo, L. Wang, T. Wu, Z. Zhang, D. Borchardt, P. Feng, *J. Am. Chem. Soc.* **2010**, *132*, 11856.
[31] D. Liu, Y. Zhang, P. Xiao, B. B. Garcia, Q. Zhang, X. Zhou, Y.-H. Jeong, G. Cao, *Electrochim. Acta* **2009**, *54*, 6816.
[32] M. Xing, J. Zhang, F. Chen, B. Tian, *Chem. Commun.* **2011**, *47*, 4947.
[33] S.-T. Myung, M. Kikuchi, C. S. Yoon, H. Yashiro, S.-J. Kim, Y.-K. Sun, B. Scrosati, *Energy Environ. Sci.* **2013**, *6*, 2609.
[34] Y. Ren, J. Li, J. Yu, *Electrochim. Acta* **2014**, *138*, 41.
[35] W. J. H. Borghols, M. Wagemaker, U. Lafont, E. M. Kelder, F. M. Mulder, *Chem. Mater.* **2008**, *20*, 2949.
[36] K. Li, S. Gao, Q. Wang, H. Xu, Z. Wang, B. Huang, Y. Dai, J. Lu, *ACS Appl. Mater. Interfaces* **2015**, *7*, 9023.
[37] X. Xin, X. Zhou, J. Wu, X. Yao, Z. Liu, *ACS Nano* **2012**, *6*, 11035.
[38] C. Han, D. Yang, Y. Yang, B. Jiang, Y. He, M. Wang, A.-Y. Song, Y.-B. He, B. Li, Z. Lin, *J. Mater. Chem. A* **2015**, *3*, 13340.
[39] N. A. Milne, M. Skyllas-Kazacos, V. Luca, *J. Phys. Chem. C* **2009**, *113*, 12983.
[40] J. Kong, Y. Wei, C. Zhao, M. Y. Toh, W. A. Yee, D. Zhou, S. L. Phua, Y. Dong, X. Lu, *Nanoscale* **2014**, *6*, 4352.
[41] A. R. Armstrong, G. Armstrong, J. Canales, R. García, P. G. Bruce, *Adv. Mater.* **2005**, *17*, 862.
[42] Y. S. Hu, L. Kienle, Y. G. Guo, J. Maier, *Adv. Mater.* **2006**, *18*, 1421.
[43] J. Maier, *Solid State Ionics* **2002**, *148*, 367.
[44] R. A. De Souza, *Phys. Chem. Chem. Phys.* **2009**, *11*, 9939.
[45] K.-S. Park, K.-M. Min, Y.-H. Jin, S.-D. Seo, G.-H. Lee, H.-W. Shim, D.-W. Kim, *J. Mater. Chem.* **2012**, *22*, 15981.
[46] B. Zhao, R. Cai, S. Jiang, Y. Sha, Z. Shao, *Electrochim. Acta* **2012**, *85*, 636.
[47] T. Xia, W. Zhang, Z. Wang, Y. Zhang, X. Song, J. Murowchick, V. Battaglia, G. Liu, X. Chen, *Nano Energy* **2014**, *6*, 109.
[48] L. Sun, J. Wang, K. Jiang, S. Fan, *J. Power Sources* **2014**, *248*, 265.
[49] B. A. Boukamp, *Solid State Ionics* **1986**, *20*, 31.
[50] M. Umeda, K. Dokko, Y. Fujita, M. Mohamedi, I. Uchida, J. R. Selman, *Electrochim. Acta* **2001**, *47*, 885.
[51] Y. C. Yang, B. H. Qiao, X. M. Yang, L. B. Fang, C. C. Pan, W. X. Song, H. S. Hou, X. B. Ji, *Adv. Funct. Mater.* **2014**, *24*, 4349.
[52] W. Song, X. Ji, Y. Yao, H. Zhu, Q. Chen, Q. Sun, C. E. Banks, *Phys. Chem. Chem. Phys.* **2014**, *16*, 3055.
[53] X.-Y. Yu, H. B. Wu, L. Yu, F.-X. Ma, X. W. Lou, *Angew. Chem. Int. Ed.* **2015**, *54*, 4001.
[54] Z. Hong, M. Wei, T. Lan, G. Cao, *Nano Energy* **2012**, *1*, 466.
[55] D. Wang, D. Choi, J. Li, Z. Yang, Z. Nie, R. Kou, D. Hu, C. Wang, L. V. Saraf, J. Zhang, I. A. Aksay, J. Liu, *ACS Nano* **2009**, *3*, 907.
[56] T. Lan, Y. Liu, J. Dou, Z. Hong, M. Wei, *J. Mater. Chem. A* **2014**, *2*, 1102.